INFRARED OBSERVATIONS DURING THE SECONDARY ECLIPSE OF HD 209458b. I. 3.6 MICRON OCCULTATION SPECTROSCOPY USING THE VERY LARGE TELESCOPE[1]

L. Jeremy Richardson,[2,3,4] Drake Deming,[2] Guenter Wiedemann,[5] Cedric Goukenleuque,[2,6]
David Steyert,[2,6,7] Joseph Harrington,[8] and Larry W. Esposito[3]

ABSTRACT

We search for an infrared signature of the transiting extrasolar planet HD 209458b during secondary eclipse. Our method, which we call "occultation spectroscopy," searches for the disappearance and reappearance of weak spectral features due to the exoplanet as it passes behind the star and later reappears. We argue that at the longest infrared wavelengths, this technique becomes preferable to conventional "transit spectroscopy." We observed the system in the wing of the strong ν_3 band of methane near 3.6 μm during two secondary eclipses, using the VLT/ISAAC spectrometer at a spectral resolution of 3300. Our analysis, which utilizes a model template spectrum, achieves sufficient precision to expect detection of the spectral structure predicted by an irradiated, low-opacity (cloudless), low-albedo, thermochemical equilibrium model for the exoplanet atmosphere. However, our observations show no evidence for the presence of this spectrum from the exoplanet, with the statistical significance of the nondetection depending on the timing of the secondary eclipse, which depends on the assumed value for the orbital eccentricity. Our results reject certain specific models of the atmosphere of HD 209458b as inconsistent with our observations at the 3 σ level, given assumptions about the stellar and planetary parameters.

Subject headings: binaries: eclipsing — planetary systems — stars: individual (HD 209458) — techniques: spectroscopic

1. INTRODUCTION

The discovery of the transiting extrasolar planet HD 209458b (Charbonneau et al. 2000; Henry et al. 2000) has provided a unique opportunity to deduce the physical characteristics of one example of the so-called hot Jupiter class of exoplanets. The transit geometry has allowed an accurate derivation of the stellar and planetary mass and radius (Brown et al. 2001b) and also provides an opportunity to measure the composition of the exoplanet atmosphere. The scale height of an atmosphere in hydrostatic equilibrium is proportional to T/g, where T is the atmospheric temperature and g is the surface gravity. Because stellar irradiation of the planet is intense at 0.046 AU (Seager & Sasselov 1998), the atmosphere could be as hot as $T \sim 1400$ K or more. Coupled with the relatively low surface gravity ($g = 848$ cm s^{-2}), the atmospheric scale height is potentially as large as $H \sim 750$ km. Moreover, when viewed tangent to the limb, the atmosphere can be opaque over several scale heights at the wavelength of a strong absorption line. The effective absorbing area of the planet can thus be greater in a strong line by a detectable amount, producing a slightly deeper eclipse at wavelengths close to the line core (Seager & Sasselov 2000; Brown 2001; Hubbard et al. 2001). That is, the opacity of the exoplanet atmosphere will impose weak, but potentially detectable, absorption lines on the stellar spectrum as the planet passes in front of the star. Several investigators have attempted to detect this effect (Bundy & Marcy 2000; Moutou et al. 2001). Using the *Hubble Space Telescope* to observe the primary eclipse, Charbonneau et al. (2002) succeeded in detecting the sodium doublet in the atmosphere of HD 209458b.

In addition to sodium, absorption in molecular features of water, methane, and carbon monoxide may also be observable (Hubbard et al. 2001; Brown 2001). Brown, Libbrecht, & Charbonneau (2002) attempted to detect absorption by carbon monoxide using ground-based observations. From their attempt and our own experience, we recognize that the terrestrial atmosphere can potentially frustrate such efforts, but we believe that good observing conditions and appropriate observational and analytical techniques will enable successful measurements from the ground. The known timing of the transit (Brown et al. 2001b) is a boon to this technique because it discriminates against false signals by providing a temporal modulation on the signal.

In this paper we introduce a new observational approach involving the *secondary eclipse*, when the planet passes behind the star. The importance of the secondary eclipse was first pointed out by Charbonneau et al. (2000), but no measurement attempt has been reported in the literature. We have performed moderate-resolution "occultation spectroscopy" to measure the modulation (i.e., disappearance and reappearance) of the potential exoplanet line spectrum as the planet is hidden and revealed by the star. We have

[1] Based on observations collected at the European Southern Observatory, Chile (proposal 67.C-0196).

[2] NASA Goddard Space Flight Center, Planetary Systems Branch, Code 693, Greenbelt, MD 20771; lee.richardson@colorado.edu, ddeming@pop600.gsfc.nasa.gov, cedric@pseudonomen.gsfc.nasa.gov, steyert@lepvax.gsfc.nasa.gov.

[3] Laboratory for Atmospheric and Space Physics, University of Colorado, 1234 Innovation Drive, Boulder, CO 80303; larry.esposito@lasp.colorado.edu.

[4] Department of Physics, University of Colorado at Boulder, Campus Box 390, Boulder, CO 80309.

[5] Astrophysikalisches Institut und Universitats-Sternwarte, D-07745 Jena, Germany; gwiedema@astro.uni-jena.de.

[6] NAS/NRC Research Associate.

[7] Joint Center for Earth Systems Technology, University of Maryland, Baltimore County, Academic IV, A-Wing, Room 114, 1000 Hilltop Circle, Baltimore, MD 21250.

[8] Department of Astronomy, Cornell University, 512 Space Sciences Building, Ithaca, NY 14853-6801; jh@oobleck.astro.cornell.edu.

also performed lower resolution spectroscopy during and near secondary eclipse using the NASA Infrared Telescope Facility (IRTF), attempting to isolate the broad infrared (IR) flux peaks from the planet's presumably hot atmosphere at wavelengths where the opacity is minimal. This paper introduces the concept of occultation spectroscopy for extrasolar planets and reports the Very Large Telescope (VLT) spectroscopic results; lower resolution occultation spectroscopy of the IR flux peaks using the IRTF observations will be the subject of a second paper.

2. OCCULTATION SPECTROSCOPY

In this section we briefly explain our rationale for attempting occultation spectroscopy at secondary eclipse, as opposed to more conventional transmission spectroscopy during primary eclipse. At visible and near-IR wavelengths, the self-emitted flux of the planet is negligible, making occultation spectroscopy of thermal emission impossible. However, many of the strongest molecular features of interest in exoplanets (e.g., the very strong fundamental ν_3 band of methane) occur at longer IR wavelengths. With increasing wavelength, the total signal detectable using occultation spectroscopy becomes as large as, or larger than, that from transit spectroscopy. To see this, consider a spectral line having sufficient strength to be opaque N scale heights higher in the atmosphere compared to the nearby continuum when viewed tangent to the limb. Cases of interest are for large N, so we can safely assume that the line is also optically thick when viewed at normal incidence to the exoplanet atmosphere. Transit spectroscopy looks for this absorption against a stellar continuum flux proportional to $\sim 2\pi R N H B_\lambda^*$, where H is the atmospheric scale height of the exoplanet, $2\pi R N H$ is the area of the annulus of the planetary atmosphere, and B_λ^* is the Planck function for the stellar continuum temperature at wavelength λ. Occultation spectroscopy, on the other hand, looks for the modulation of the exoplanet spectrum itself, with continuum flux proportional to $\sim \pi R^2 B_\lambda^p$, where B_λ^p is the Planck function for the exoplanet continuum temperature. With increasing wavelength, the increase in B_λ^p and the large area of the exoplanet (πR^2) dominate the area of the atmospheric annulus ($2\pi R N H$) in spite of the greater stellar intensity (B_λ^*). Evaluating the ratio of these fluxes for $N = 3$, $H = 750$ km, $R = 1.0 \times 10^5$ km, and stellar and exoplanet temperatures of 6000 and 1200 K, respectively, we find that the ratio equals unity for $\lambda = 2.6 \,\mu$m. A rigorous treatment would of course include the line profiles and many other factors, but the inevitable tendency is that, for wavelengths longward of the K photometric band, occultation spectroscopy becomes increasingly favorable over transmission spectroscopy in terms of the amplitude of the potential signal.

Occultation spectroscopy is essentially direct IR spectroscopy of the exoplanet, and in principle this could be done at most orbital phases and also for planets that do not transit. However, it requires detection of the small-amplitude exoplanet spectrum (the precise nature of which is unknown), superposed on a strong stellar background. The measurement becomes much easier if the signal is *modulated predictably*. The disappearance of the exoplanet spectrum during secondary eclipse is therefore an essential part of our technique. Note, however, that modulation by variations in Doppler velocity could also be used for all hot Jupiter systems, even ones without transits (Wiedemann,

Deming, & Bjoraker 2001). Note also that the concept of occultation spectroscopy is not new; it was successfully used to obtain the IR spectra of Pluto and its moon Charon (Sawyer et al. 1987).

3. OBSERVATIONS

We observed two secondary eclipses, on UT 2001 July 8 and UT 2001 July 15, with the ISAAC spectrometer on the VLT (Antu) at Cerro Paranal in Chile. The observations were performed in visitor mode, with real-time decisions regarding nodding frequency, integration time, etc. Both nights were clear, with 10%–20% relative humidity and seeing in the range 0″.5–0″.7. The zenith column of precipitable water vapor, as measured from telluric water lines in our spectra, was ∼6 mm on July 8 and 1.6 mm on July 15.

ISAAC is capable of imaging and spectroscopy in the wavelength region between 1 and 5 μm (Moorwood 1997). We used spectroscopic mode with a resolving power of 3300, covering the 3.5–3.75 μm range (2667–2852 cm^{-1}). Both eclipses occurred within an hour of transit across the local meridian, where the star reached a minimum air mass of 1.38. The spectra maintained good quality to the largest air mass we observed (2.51).

At approximately half-hour intervals, we observed a comparison star, HD 210483. The comparison star is within a degree of HD 209458, with nearly the same B and V magnitudes and photometric colors (Table 1). We observed both stars using a conventional "nod" technique, placing them alternately at "a" and "b" positions on the slit, in the order "abba," with 60 s integrations at each slit position. On July 8 we obtained 36 "abba" sets of HD 209458 and 20 "abba" sets of HD 210483, while on July 15 we recorded 41 and 24 sets, respectively. About once per hour, we obtained spectra of a continuum lamp for flat-fielding. We did not rely on the standard flats; instead, we recorded flat-field exposures immediately after each block of HD 209458 observations without moving the telescope or instrument, in order to avoid small but nonnegligible flexure effects.

4. MODELED SPECTRUM

We do not expect to achieve sufficient precision to detect the planetary spectrum in each individual spectral resolution element; instead, we look for the candidate signal by performing a least-squares fit of the observations to a model " template." We computed the template as the emergent flux from a model atmosphere for the exoplanet, using a series of specific intensity spectra at different values of μ (the cosine of the zenith angle). These were computed from the formal

TABLE 1
STELLAR PHOTOMETRIC DATA

Parameter	HD 209458	HD 210483
V[a]	7.648	7.586
$B-V$[a]	0.594	0.585
$b-y$[b]	0.361	0.391
m_1[b]	0.174	0.175
c_1[b]	0.362	0.354

[a] *Hipparcos* Catalogue (Perryman et al. 1997).
[b] *uvbyβ* Photometric Catalogue (Hauck & Mermilliod 1998).

integral of the radiative transfer equation, using an LTE source function; we neglected all scattering terms, since the long-wavelength region is of interest and we are assuming a cloud-free model. Flux was computed by a quadrature integration of the intensity spectra. The spectrum synthesis was done at very high spectral resolution and convolved to the 0.8 cm^{-1} resolution of our ISAAC data using a Gaussian instrument profile. We adopted the parameters for the star and planet given by Cody & Sasselov (2002).

Model atmospheres for the planet can vary widely, with one major difference being the treatment of clouds and aerosols. The maximum thermal contrast in IR spectra is generally obtained from clear atmospheres; one reason for this is the fact that scattering processing in clouds tends to wash out strong absorption features. Moreover, the presence of clouds high in the atmosphere effectively limits the detection of methane by allowing only the small fraction of the column above the cloud to be probed by the observer. We have therefore used the most optimistic case of the clear atmosphere as a reference point. Our fiducial model follows the calculation of Goukenleuque et al. (2000), with the surface gravity appropriate for HD 209458b. This model includes irradiation by the star but uses only gaseous opacities; condensates and particulates are assumed to have settled out of the atmosphere forming a deep cloud layer. Figure 1 compares the pressure/temperature structure from our fiducial model with a recent model from S. Seager (2002, private communication). The temperature versus optical depth structures of these models are similar, but the fiducial model requires a much higher pressure (as a result of lower opacity) to attain the same optical depth as the Seager model. We also inspected a model for HD 209458b kindly sent to us by D. Sudarsky (2002, private communication); it is slightly hotter than the Seager model at all depths.

We calculated the number densities of methane in the fiducial model, using the simple analytic formulae given by Burrows & Sharp (1999). The methane mixing ratio peaks at $\sim 7 \times 10^{-6}$ at 25 mbar pressure, similar to the values for the 51 Peg model (Goukenleuque et al. 2000). In computing the template, we used the current best available experimental methane line parameters from Brown, Dulick, & Devi

(2001a), now incorporated into HITRAN (Rothman et al. 1998), and the calculation followed Wiedemann et al. (2001) in other respects (partition functions, etc.). Since line parameters are critical to calculation of the template, we calculated spectra of hot methane (773 K) at ISAAC resolution for laboratory conditions, using both our adopted line data and also theoretical line parameters from the spherical top data system theory (Wenger & Champion 1998). We compared these calculated spectra to laboratory measurements of hot methane at 773 K, measured by D. Steyert & D. Reuter (2002, private communication) at the same resolution. Based on this comparison, we have confidence in the HITRAN methane line data used to compute our model spectrum. Since our spectral region also exhibits absorption due to water, we experimented using water lines in our template, also based on HITRAN. Because the HITRAN database is incomplete at high temperatures, we also experimented with using HITEMP, a HITRAN line database extension for higher temperatures, to obtain water line data. This results in abundant weak absorption lines that do not significantly change the template. We have therefore neglected water absorption in the analysis until more complete information is available for individual hot water lines in this spectral region.

We expressed the exoplanet flux spectrum as a ratio to the stellar flux. We computed the stellar flux from a gray atmosphere at $T = 5800$ K, reducing the adopted 6000 K stellar temperature by 200 K to allow for the decrease in brightness temperature from the visible to 3.6 μm, as documented for the solar spectrum by Vernazza, Avrett, & Loeser (1976).

Figure 2 shows the modeled template spectrum, with and without water lines from HITRAN included. In the results quoted and discussed below, we have used the "methane only" version of the model template, for reasons given above. However, our results and associated errors do not change significantly if "HITRAN water" or "HITEMP water" is included in the model template.

We computed methane spectra from models intermediate between our fiducial model and the Seager model. If we increase the continuous opacity in the fiducial model, while preserving the same temperature–optical depth relation, the
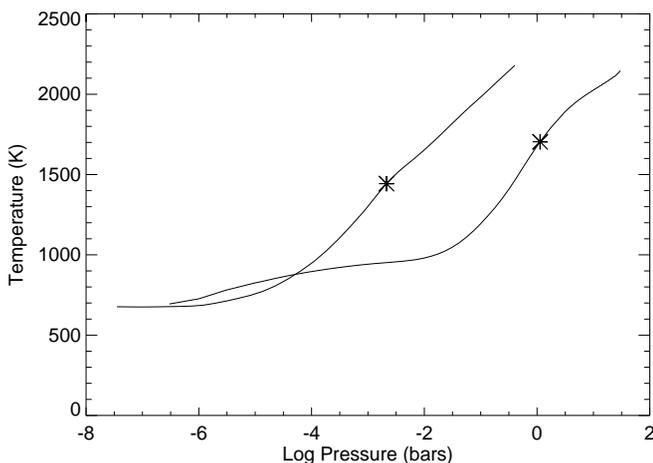

Fig. 1.—Temperature vs. pressure structure for our fiducial model for HD 209458b (*rightmost curve*) and for a model by S. Seager (2002, private communication). The asterisks mark the points of Rosseland optical depth unity (Seager model) and 3.6 μm optical depth unity (fiducial model).
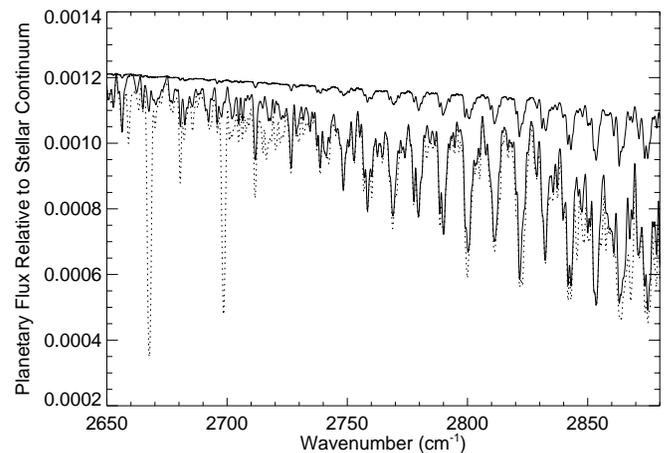

Fig. 2.—Model template spectra containing only methane lines (*lower solid curve*) and both methane and water lines (*dotted curve*). The upper solid curve represents the methane only template with a factor of 3 increase in the continuous opacity, but retaining the same temperature–optical depth relation.

methane bands weaken rapidly (see Fig. 2). The greater continuous opacity pushes all line formation to lower pressure layers, giving lower column densities "above the continuum." The mixing ratio of methane decreases at low pressures (Burrows & Sharp 1999), further lowering the methane column density. Our fiducial model is a limiting case of an exceptionally clear atmosphere, and many other models for the exoplanet will not exhibit significant methane features, thereby escaping the test of our present analysis.

5. DATA ANALYSIS

Analysis of the HD 209458 observations took place in four stages: (1) extraction of spectra from the two-dimensional data frames, (2) removal of the telluric (and the few intrinsically stellar) absorption features from the spectra, yielding residuals that potentially contain the exoplanet spectrum, (3) estimation of the "amplitude" of the exoplanet's spectrum in each residual spectrum, and (4) fitting of the aggregate results to a secondary eclipse curve. Since our present (and future) results depend critically on the fidelity of our data analysis, we describe this process in some detail, and we also describe checks made to ensure the integrity of the analysis.

5.1. *Spectral Extraction*

The spectral frames were first cleaned of "hot pixels" and temporary anomalies such as energetic particle events. Temporal sequences of frames at a single nod position were examined to locate hot pixels based on their variability, and these pixels were given zero weight in subsequent analysis. Energetic particle events were identified and repaired separately using a median filter applied to the temporal sequence. The cleaned "abba" set was combined by adding the "a" frames and subtracting the "b" frames to produce a difference image, which was then divided by a flat-field frame. The flat-field frame was computed as an average of the individual flats during the night. We verified that temporal variations in the flats were negligible for purposes of our analysis.

At an excellent IR site such as Paranal, changes in the thermal background are approximately linear with time during the several minutes required to record an "abba" set. Consequently, most of the background emission is removed by construction of the difference image $a - b - b + a$. However, we found that a second-order correction was necessary to remove the background completely. We compute the residual background spectrum by summing the region between the "a" and "b" slit positions in the difference image. The relatively long slit used in ISAAC facilitates the precision of this correction by providing a $17''$ length of background. This residual background spectrum is subtracted from each row of the two-dimensional difference image prior to the extraction of the spectra. Note that our technique differs from usual IR practice, which would be to subtract the (negative) "b" spectrum from the "a" spectrum after their extraction from the difference image, which would automatically subtract the background to second order. However, this would not maintain separate "a" and "b" spectra, which we desired in order to verify that our results are independent of the position of the spectra on the detector array.

We extracted the "a" and "b" spectra from the difference image using the optimal extraction formalism of Horne (1986). The spatial profile needed in the optimal extraction was constructed by fitting polynomials in the intensity-versus-wavelength distribution at each slit position and then sampling these curves in the spatial direction at each wavelength. In the process of extracting the spectra, we noted that the approximate signal-to-noise ratio of each spectrum ($\sim$200) was close to the value expected based on the noise from Poisson statistics of photoelectrons from the background.

At this stage of the analysis, the spectra were separated into sets corresponding to July 8 or July 15, HD 209458 or HD 210483, and "a" or "b" slit positions. Each of the eight sets was analyzed independently of the other sets. The individual spectra in each set were shifted slightly using spline interpolation, so that the telluric absorption features were all coincident. Frequencies in wavenumber for the telluric lines were derived from high-resolution solar Fourier transform spectra (Livingston & Wallace 1991), convolved down to the resolution of the ISAAC data. (This accounted for any blending of telluric lines, which can change their effective wavenumbers.) Wavenumbers for each point in our ISAAC spectra were derived by spline interpolation using the telluric lines as standards; the error of this procedure was $\sim$0.1 cm^{-1}, much less than the 0.8 cm^{-1} spectral resolution. A single accurate wavenumber scale was thereby inferred for all the spectra in each set. Sample spectra from both nights are shown in Figure 3.

5.2. *Telluric Correction*

The intensities in each spectrum fluctuate as a result of variable losses at the ISAAC slit, as well as changes in the telluric line and continuum absorption. For each set of spectra, we made an intensity normalization, followed by a correction to remove the telluric absorption. A pseudocontinuum was used as an aid to normalization; it was determined as a spline fitted to a set of points in each spectrum having the greatest intensity in predetermined wavenumber intervals. We then used a wavelength-independent scale factor to normalize each spectrum so that the integral intensity under the pseudocontinuum was constant for all spectra. That is, we enforce the condition that the total intensity under each pseudocontinuum is equal to the total intensity under the average pseudocontinuum; the normalization factor f_i is calculated from

$$f_i = \frac{\sum_\lambda \bar{c}}{\sum_\lambda c_i} , \qquad (1)$$

where $\bar{c}$ represents the average pseudocontinuum, c_i represents the fitted pseudocontinuum to spectrum i, and f_i is the factor by which each spectrum i is multiplied. Thus, the normalized spectra are calculated by

$$n_i = f_i s_i , \qquad (2)$$

where n_i is the normalized spectrum and s_i is the original spectrum.

In the normalized spectra, at each wavelength element, we fit a least-squares line to the natural log of intensity with air mass, $\ln n_i(x, \lambda)$. The fitted slope b_λ was used to correct
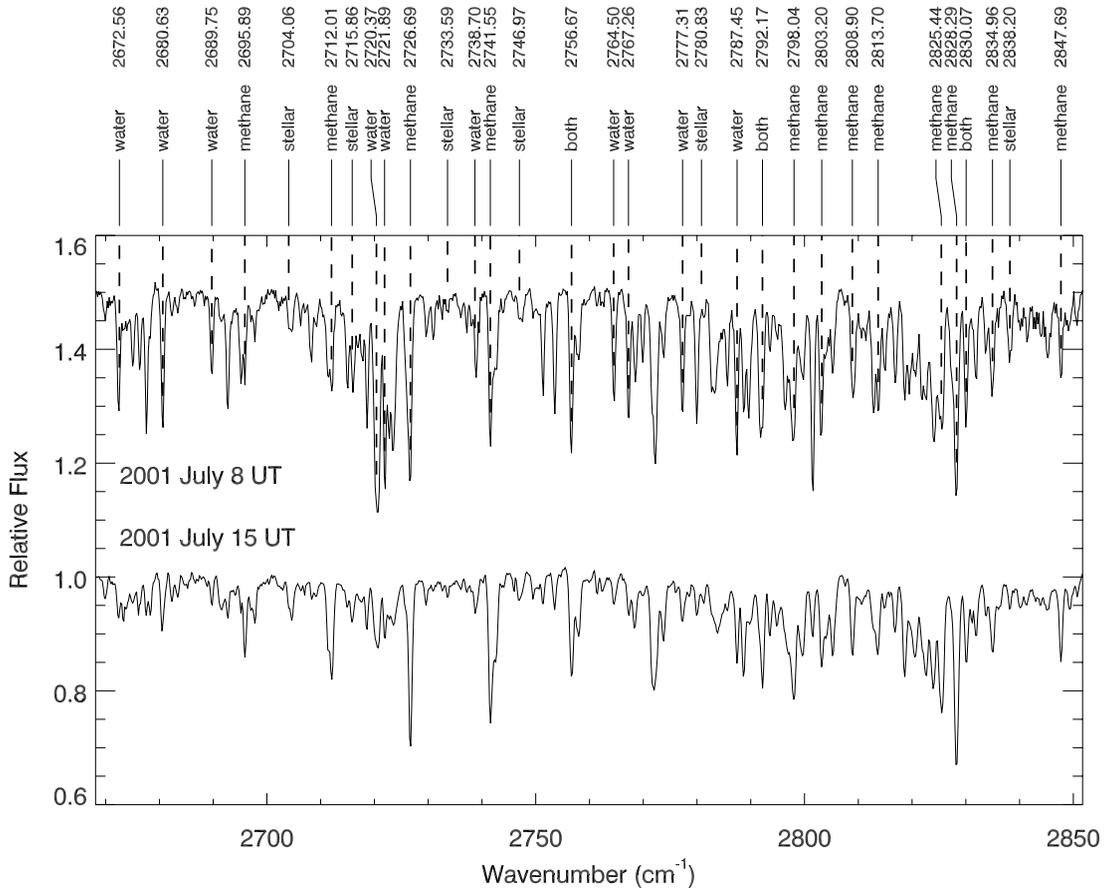
Fig. 3.—Sample spectra of HD 209458 for both observing nights. Most of the line structure is telluric, as a result of methane and water vapor, as noted by the line identifications. A few stellar lines are also marked (Farmer 1989). Note that the telluric water vapor lines were stronger on 2001 July 8. The spectrum from 2001 July 8 has been shifted by +0.5 for plotting purposes.

each intensity value to the minimum air mass in that set of spectra (this corrects for air-mass–dependent telluric absorption). That is, the air-mass–corrected spectrum n'_i is obtained from

$$n'_i = \exp[\ln n_i(x, \lambda) - b_\lambda(x - x_{\min})] \ . \qquad (3)$$

Each set of corrected spectra was then averaged. Residual spectra were calculated by subtracting the average spectrum and dividing the difference by a continuum fitted to the average spectrum. This produced residual spectra given by

$$r_i = \frac{n'_i - \bar{n}'}{c_{\bar{n}'}} \ , \qquad (4)$$

which presumably contain the candidate exoplanet signal.

It is important to note several properties of the residual spectra. Division by the pseudocontinuum of the average spectrum leaves the residuals expressed in units of the stellar continuum. However, since we divided by only one continuum curve per data set, temporal changes in intensity were not masked by fluctuating errors in continuum fits. In addition, the subtraction of the average spectrum means that the sum of the residuals at each wavelength is identically zero. Thus, only variations in the spectra survive this process. In particular, the exoplanet spectrum will survive (since it varies as a result of the eclipse), but the intrinsically stellar lines (Farmer 1989) are subtracted.

5.3. Higher Order Corrections

Several additional corrections were needed before the residuals could be compared with the model spectrum. First, we noticed that a broad absorption feature was evident in some of the residual spectra, and it corresponded to a blend of water lines near 2720 cm^{-1}. The depth of this feature relative to the stellar continuum was ~30% greater on the more humid night (July 8), and variations of the depth of the feature on either night were about ±2%. To correct these variations, we obtained a low-noise residual water spectrum by differencing the natural logarithms of the average spectrum for July 8 and July 15 (for both stars, and for both the ``a'' and ``b'' spectra, separately). This exploits the (fortuitous) fact that the precipitable water vapor column was appreciably different on the two nights, but telluric methane absorption was the same. (Unlike the concentration of water in the troposphere, which is highly variable, methane is effectively constant because it is long lived and therefore well mixed.) We tested each residual spectrum to see whether a significant correlation existed with the water vapor spectrum. If it did, then we removed it from the residuals by least-squares fitting.

We also noticed that the residuals sometimes exhibit variations at low spatial frequencies (see Fig. 4, *upper panel*). These baseline effects (typically ~0.2%–0.3%) are not surprising because our analysis treats each wavelength point independently. (We do not introduce artificial baselines,
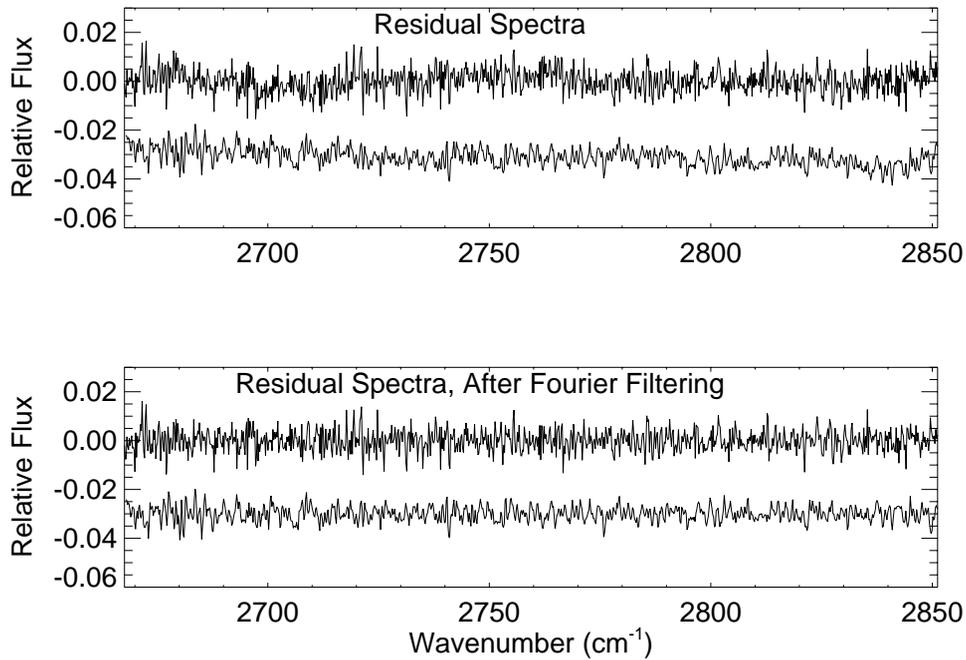
FIG. 4.—Residual spectra corresponding to the example spectra shown in Fig. 3. *Upper:* Residuals from the extracted spectra after telluric correction. *Lower:* Same residuals after the Fourier filtering process. The residual spectrum from July 15 (*lower curve*) has been shifted by −0.03 for plotting purposes.

e.g., by continuum fitting, but neither do we suppress real baseline variations.) A Fourier analysis also revealed a spike of excess power at the Nyquist frequency (0.5 cycles pixel^{-1}), which is commonly seen in IR data, usually indicating a difference in the two output amplifiers reading alternate columns of the detector array. We removed these effects by computing the Fourier transform for each set of residuals; then we zeroed out an appropriate number of low-frequency elements, as well as the DC offset (zero frequency) and the Nyquist frequency components. The number of low frequencies removed (up to 0.0079 cycles pixel^{-1}) was taken to be the maximum possible without impinging on frequencies where the exoplanet model spectrum exhibited significant power. The same filter operations were performed on the model template spectrum as on the observed residuals. Then we inverse-transformed the filtered residuals and template, which were then suitable for comparison. The effect of this Fourier filtering on the observed residuals is seen in the lower panel of Figure 4.

Even after the removal of variable water vapor absorption and Fourier filtering, the residuals needed an additional correction. We discovered that they contained an excess of "outliers," i.e., points more than several standard deviations from zero. We exploited our comparison star observations to find those wavelengths that tended to become outliers and reject them from the analysis. The procedure was applied to the "a" and "b" spectra separately, since we suspected low-amplitude hot pixels as a likely cause of outliers. We applied a wavelength-dependent "weighting mask" to the residuals, where the weight of the mask (normally unity) was set to zero when a particular wavelength was found to deviate from zero by more than 2.5 σ in two or more spectra for both HD 209458 and HD 210483. The requirement that points are zero-weighted only if that wavelength tends to be discrepant in spectra from *both* stars assures that this procedure does not bias the results. About

7% of the points were zero-weighted using this method; we found that our final results were remarkably insensitive to the limits for the rejection. The reason for this is that the total number of outliers was much less than 7% because a given point was always zero-weighted when it met the above criterion, even if it was "well behaved" in the majority of spectra. The standard deviation of the Fourier-filtered and masked residual spectra was in the range 0.003–0.006.

5.4. *Fit to the Exoplanet Spectrum*

Prior to fitting the model template and Fourier filtering, the residuals are corrected for the heliocentric Doppler shift due to the relative motion of HD 209458 with respect to the Sun (Nidever et al. 2002), as well as the geocentric Doppler shift due to the relative motion of the Earth around the Sun. We have also corrected for the nonnegligible Doppler shift due to the orbital motion of the exoplanet with respect to HD 209458. The residuals are shifted in wavenumber to the rest frame of the exoplanet, and the model spectrum (already in the exoplanet rest frame) is interpolated onto the same wavenumber grid. Note that although the correction is small, we have corrected each residual (each frame) for the Doppler effect, based on its time of observation. The residuals calculated for HD 210483 are analyzed in an identical manner. Although HD 210483 is not known to host a planet, we apply the same Doppler correction as we did to HD 209458, but we calculate the correction based on the time of observation of each HD 210483 residual.

The comparison between each residual spectrum and the model exoplanet spectrum is made using linear least squares. For this purpose we use the methane only version of the model (see § 4), since the state of the spectroscopic line data gives us the most confidence in this version. (Our overall results do not change with the "methane plus water" version.) The result of a least-squares regression of the residuals versus the model spectrum gives a quantitative estimate

of the degree to which each residual spectrum "contains" the exoplanet model spectrum. We refer to these estimates as "model amplitudes," since they represent the degree to which the model spectrum appears in each residual spectrum. The least-squares fit also estimates the random error in the model amplitudes, typically 1.5–2.5. In other words, the signal-to-noise ratio for detecting the modeled exoplanet spectrum in a single set of residuals is about 0.5. This is sufficient precision to expect detection of the exoplanet spectrum in the average of ∼50 residual spectra, provided that the signal-to-noise ratio increases as the square root of the number of spectra averaged.

5.5. Checks on the Analysis

We have checked our analysis procedures in several ways. Since we use linear least squares, the analysis should have the property that averaging the best-fit model amplitudes for a set of residual spectra should give the same result as fitting to the average of those residual spectra. We verified that our results satisfy this identity exactly, *if* the time-variable Doppler shift applied to the residuals is neglected (with Doppler shifts included, the equality is approximate). We have also confirmed that our numerical procedures do not attenuate potential signals. We added a synthetic signal, identical to the modeled spectrum, at the earliest practical stage of the analysis (immediately after the extraction of the spectra from the two-dimensional data frames). The least-squares solutions recover this signal (as a difference, out of eclipse minus in eclipse) with a best-fit model amplitude of near unity.

Another important check on our analysis is to examine the nature of the noise, specifically the distribution of noise as compared to a normal error distribution. This is important because our error estimates implicitly assume that the data reflect a normal error distribution. Figure 5 shows the error distribution for all of the points (after masking) in the "a" residuals of HD 209458 from July 8. Apart from an excess of points within 1 σ of zero, the distribution closely approximates a normal error curve. Similar distributions are found for the other sets of data.

Figure 6 shows the distribution of model amplitudes. In this case we construct the distribution from the least-
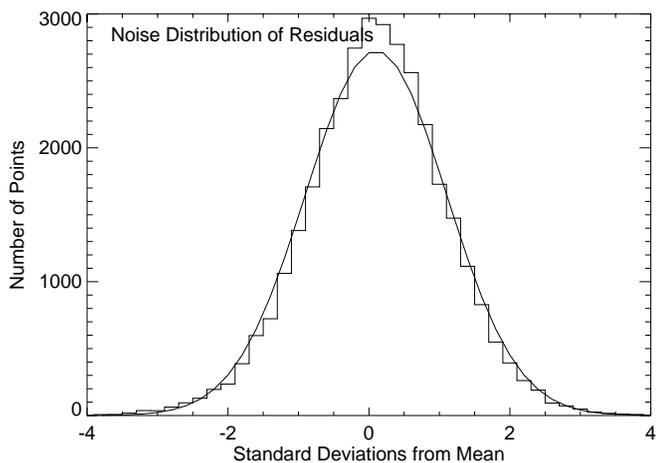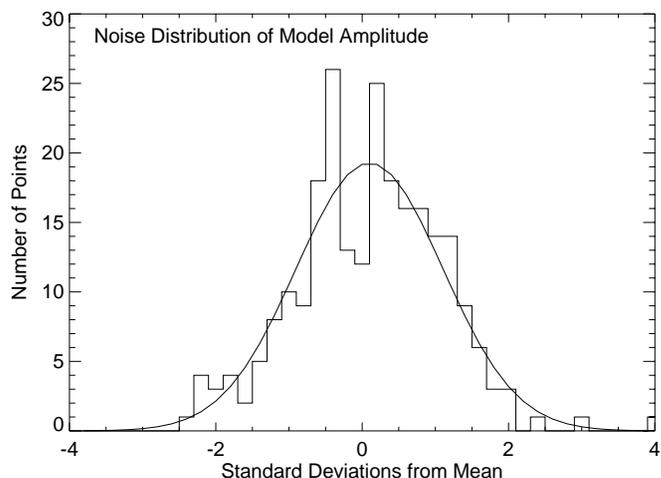

Fig. 6.—Noise distribution for computed values of model amplitude. All measurements (242) are included: both stars, both nights, and for both the "a" and "b" spectra. The solid line indicates the theoretical value based on the Gaussian probability distribution.

squares fits to all residual spectra for both HD 209458 and HD 210483 from both nights; this comprehensive inclusion is needed to provide sufficient points to expect a reasonable approximation to the normal error curve. Considering the number of residual spectra represented (242), the data are in good agreement with the normal error curve. As a further check on the errors, we computed the variation in fitted model amplitudes that result from fitting Gaussian random noise whose standard deviation varied from 0.003 to 0.006, the same as the range of our filtered and masked residuals. The results of this simulation were in close agreement with the error estimates derived from the least-squares fits to the actual residual data.

5.6. Secondary Eclipse Timing

The timing of secondary eclipse depends on the orbital eccentricity. If the eccentricity is identically zero (as might be expected based on tidal circularization arguments), the secondary eclipse will occur exactly midway between primary eclipses. If the eccentricity is nonzero, it can occur up to ∼90 minutes earlier or later (depending also on ω). Doppler observations to date (G. W. Marcy 2002, private communication) give $e = 0.011 \pm 0.015$ with $\omega = 156°$, which would imply $\delta t = -31$ minutes, i.e., a slightly earlier secondary eclipse. We computed the time of secondary eclipse as a function of the eccentricity, using $P = 3.52474$ days (G. W. Marcy 2002, private communication) and the zero point from primary eclipse at $T_0 = 2,451,659.93675$ HJD (Brown et al. 2001b), and we corrected for light-travel time. We checked our calculations against a primary eclipse ephemeris by D. Charbonneau,[9] obtaining essentially identical results, and we did a similar check for the time difference introduced by using a nonzero eccentricity (D. Charbonneau 2002, private communication). Given a calculated time for secondary eclipse, we fit a simple eclipse curve to our model amplitude data by linear least squares. Our eclipse curve uses two levels (in and out of eclipse) connected by straight lines. The time from first to fourth contact was taken to be 184.3 minutes, and from second to

Fig. 5.—Noise distribution of the residuals for the target "a" spectra on UT 2001 July 8. The solid line indicates the theoretical value based on the Gaussian probability distribution.

---

[9] See http://www.astro.caltech.edu/~dc/frames.html.

third contact 132.2 minutes (Charbonneau et al. 2002). Note that, as a result of the subtraction of an average spectrum in our data analysis, only the *amplitude* of the eclipse curve is significant; the zero point in the fitted eclipse curve is not meaningful.

6. RESULTS AND DISCUSSION

Given the precision achieved by our analysis, we would expect to detect the exoplanet spectrum if it is represented by the irradiated, cloudless, low-albedo atmosphere, with thermochemical equilibrium abundances of methane (and water), and also provided that the timing of the secondary eclipse is known and the stellar and exoplanet parameters (radii, etc.) are exactly as adopted. We first conclude that this precision can indeed be achieved using ground-based observations. The recent results and discussion of Brown et al. (2002) imply that ground-based detection is feasible, since these authors came within a factor of ∼3 of the required precision using data from only one night in poor weather. Our experience, using a somewhat different technique, confirms that the requisite precision can be obtained if good observing conditions prevail.

Our results for the secondary eclipse are illustrated in Figures 7 and 8, showing the derived model amplitudes for each HD 209458 spectrum (" a " and " b " for both nights) versus time from the assumed midpoint of secondary eclipse. Recall that the error bars for individual spectra were derived from the least-squares fits to the residuals after telluric corrections, Fourier filtering, and masking. We fit an eclipse curve to the aggregate results at each assumed eclipse

time. (We fold the curve about the midpoint of secondary eclipse for the figures.) Furthermore, there is no evidence that the results from the " a " and " b " spectra analyzed separately are significantly different. Figure 7 shows the result for $e = 0.011$, i.e., taking the slightly nonzero eccentricity from the Doppler data at face value, again for all spectra. The solid line is the least-squares estimate of the eclipse amplitude, -0.1 ± 0.3, and the dashed line shows the levels corresponding to an eclipse amplitude of unity (i.e., if the model template spectrum correctly represents the exoplanet and the timing is correct). Figure 8 shows the corresponding result (0.5 ± 0.4) under the assumption that the eccentricity is identically zero. In each case the reduced χ^2 of the fit is ∼1.5, indicating that the scatter of the data is only slightly larger than the independently assigned error bars. Note that each plot for HD 209458 is accompanied by a similar fit to the comparison star, shown in the lower panels. In both cases, the comparison star shows no significant change, as expected.

Adopting $e = 0.011$ from the Doppler data, our results for nondetection of the secondary eclipse (-0.1 ± 0.3) exclude the model template spectrum at the greater than 3 σ level. Given our error distributions, this case is firmly rejected. Assuming an eccentricity of zero, nondetection of the secondary eclipse is ambiguous (0.5 ± 0.4). However, even if we explore eccentricities over the entire plausible range from 0.0 to 0.03 and assume ω-values in the first and second quadrants, the fitted secondary eclipse amplitudes never reach unity. Instead, the amplitudes vary from -0.2 to 0.9, and the amplitudes for the comparison star similarly range from -0.5 to 0.9. At a given eclipse time, the
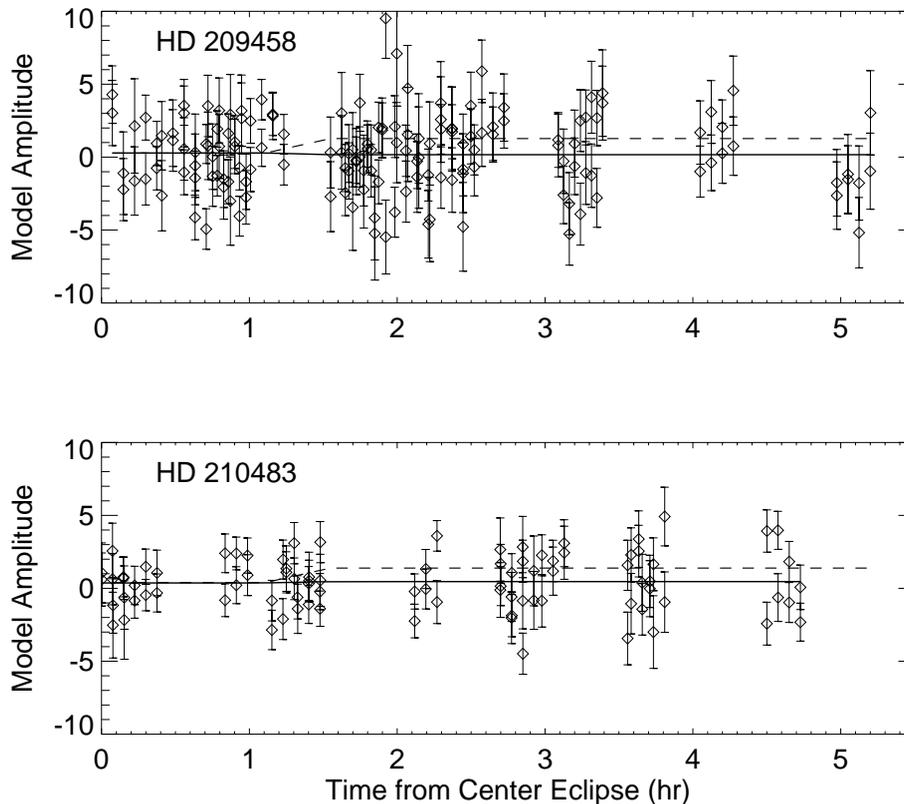

Fig. 7.—Fitted secondary eclipse curves (*solid line*) for HD 209458 (*upper panel*) and the comparison star (*lower panel*). These fits assume the current best-fit Doppler value of the orbital eccentricity, $e = 0.01$, resulting in the eclipse being 31.1 minutes earlier than that of an orbit with zero eccentricity. The dashed lines represent an eclipse amplitude of unity.
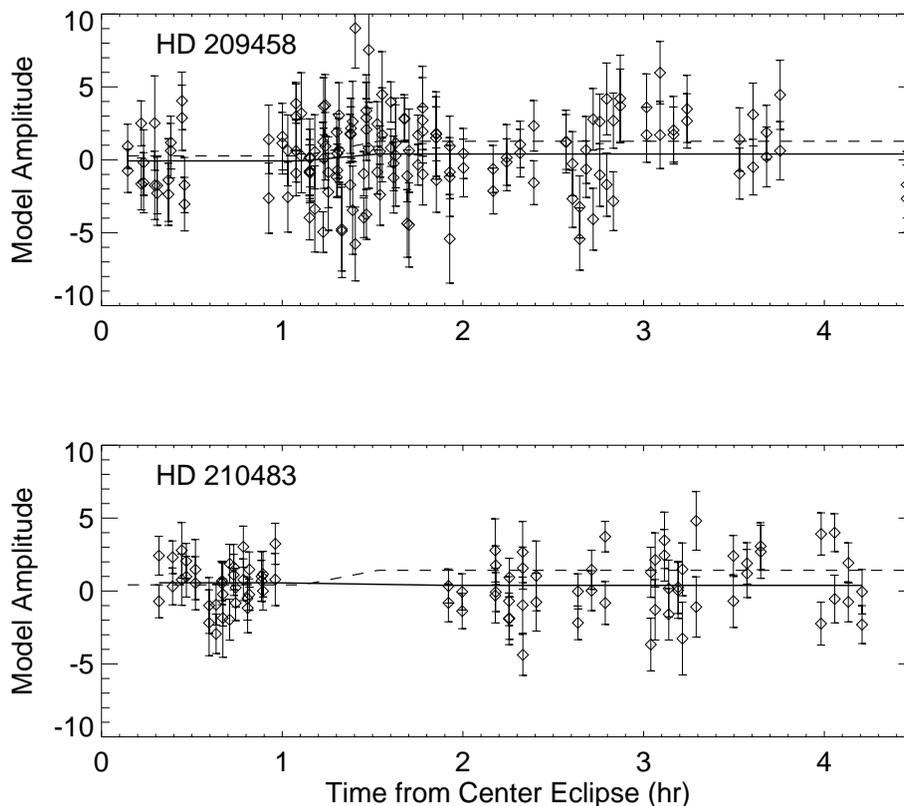
FIG. 8.—Fitted secondary eclipse curves (*solid line*) for HD 209458 (*upper panel*) and the comparison star (*lower panel*). These fits assume that the orbital eccentricity is zero. The dashed lines represent an eclipse amplitude of unity.

amplitudes for the two stars are uncorrelated, as expected when sampling the noise envelopes resulting from fitting independent random data to eclipse curves of variable timings. We therefore conclude that the secondary eclipse is not detected using our "methane template." Given the similarity between HD 209458 and the comparison star in terms of the noise envelope, and noting the nearly identical reduced χ^2 values, we conclude that HD 209458b probably does not exhibit significant methane absorption features, in agreement with the models of Sudarsky, Burrows, & Hubeny (2002). Methane absorption in the combined light spectrum (star plus planet) has a total equivalent width of no more than 0.025 cm^{-1} within our absorption bandpass (2667–2852 cm^{-1}).

Deviation of the exoplanet atmosphere from our fiducial model is not difficult to explain. As discussed in § 4, models of this exoplanet must be exceptionally clear if significant methane absorption is to appear in their spectrum. In this respect our fiducial model represents a limiting case. Our results are certainly consistent with the suggestion of a cloudy atmosphere based on the observed low sodium abundance (Charbonneau et al. 2002). However, even in a clear atmosphere there may be other viable explanations for both the sodium result (Barman et al. 2002) and our present result (e.g., photochemical depletion of methane). Nevertheless, it is significant that we can now begin to limit the range of parameters of viable exoplanet models using *ground-based* observations.

REFERENCES

Barman, T. S., Hauschildt, P. H., Schweitzer, A., Stancil, P. C., Baron, E., & Allard, F. 2002, ApJ, 569, L51
Brown, L. R., Dulick, M., & Devi, V. M. 2001a, DPS Meeting, 33, 56.11
Brown, T. M. 2001, ApJ, 553, 1006
Brown, T. M., Charbonneau, D., Gilliland, R. L., Noyes, R. W., & Burrows, A. 2001b, ApJ, 552, 699
Brown, T. M., Libbrecht, K. G., & Charbonneau, D. 2002, PASP, 114, 826
Bundy, K. A., & Marcy, G. W. 2000, PASP, 112, 1421
Burrows, A., & Sharp, C. M. 1999, ApJ, 512, 843
Charbonneau, D., Brown, T. M., Latham, D. W., & Mayor, M. 2000, ApJ, 529, L45

Charbonneau, D., Brown, T. M., Noyes, R. W., & Gilliland, R. L. 2002, ApJ, 568, 377
Cody, A. M., & Sasselov, D. D. 2002, ApJ, 569, 451
Farmer, C. B. 1989, A High-Resolution Atlas of the Infrared Spectrum of the Sun and the Earth Atmosphere from Space: A Compilation of the ATMOS Spectra of the Region from 650 to 4800 cm^{-1} (2.3 to 16 μm) (RP-1224; Washington, DC: NASA)
Goukenleuque, C., Bézard, B., Joguet, B., Lellouch, E., & Freedman, R. 2000, Icarus, 143, 308
Hauck, B., & Mermilliod, M. 1998, A&AS, 129, 431
Henry, G. W., Marcy, G. W., Butler, R. P., & Vogt, S. S. 2000, ApJ, 529, L41
Horne, K. 1986, PASP, 98, 609
Hubbard, W. B., Fortney, J. J., Lunine, J. I., Burrows, A., Sudarsky, D., & Pinto, P. 2001, ApJ, 560, 413
Livingston, W., & Wallace, L. 1991, An Atlas of the Solar Spectrum in the Infrared from 1850 to 9000 cm^{-1} (1.1 to 5.4 μm), (Tech. Rep. 91-001; Kitt Peak: NSO)

Moorwood, A. F. 1997, Proc. SPIE, 2871, 1146
Moutou, C., Coustenis, A., Schneider, J., St Gilles, R., Mayor, M., Queloz, D., & Kaufer, A. 2001, A&A, 371, 260
Nidever, D. L., Marcy, G. W., Butler, R. P., Fischer, D. A., & Vogt, S. S. 2002, ApJS, 141, 503
Perryman, M. A. C., et al. 1997, A&A, 323, L49
Rothman, L. S., et al. 1998, J. Quant. Spectrosc. Radiat. Transfer, 60, 665
Sawyer, S. R., Barker, E. S., Cochran, A. L., & Cochran, W. D. 1987, Science, 238, 1560
Seager, S., & Sasselov, D. D. 1998, ApJ, 502, L157
———. 2000, ApJ, 537, 916
Sudarsky, D., Burrows, A., & Hubeny, I. 2002, ApJ, submitted
Vernazza, J. E., Avrett, E. H., & Loeser, R. 1976, ApJS, 30, 1
Wenger, C., & Champion, J. P. 1998, J. Quant. Spectrosc. Radiat. Transfer, 59, 471
Wiedemann, G., Deming, D., & Bjoraker, G. 2001, ApJ, 546, 1068